Tensile Ge microstructures for lasing fabricated by means of a silicon complementary metal-oxide-semiconductor process

G. Capellini,[1,2,*] C. Reich,[2] S. Guha,[2] Y. Yamamoto,[2] M. Lisker,[2] M. Virgilio,[3] A. Ghrib,[4] M. El Kurdi,[4] P. Boucaud,[4] B. Tillack,[2,5] and T. Schroeder[2,6]

[1]*Dipartimento di Scienze, Università degli Studi Roma Tre, viale G. Marconi 446, I-00146 Roma, Italy*
[2]*IHP, Im Technologiepark 25, D-15236 Frankfurt (Oder), Germany*
[3]*Dipartimento di Fisica 'E Fermi', Università di Pisa, largo Pontecorvo 3, I56127 Pisa, Italy*
[4]*Institut d'Electronique Fondamentale, CNRS-Université Paris-Sud, F-91405 Orsay, France*
[5]*Technische Universität Berlin, HFT4, Einsteinufer 25, D-10587 Berlin, Germany*
[6]*Brandenburgische Technische Universität, Konrad-Zuse-Strasse 1, D-03046 Cottbus, Germany*
[*]*capellini@fis.uniroma3.it*

Abstract: In this work we study, using experiments and theoretical modeling, the mechanical and optical properties of tensile strained Ge microstructures directly fabricated in a state-of-the art complementary metal-oxide-semiconductor fabrication line, using fully qualified materials and methods. We show that these microstructures can be used as active lasing materials in mm-long Fabry-Perot cavities, taking advantage of strain-enhanced direct band gap recombination. The results of our study can be realistically applied to the fabrication of a prototype platform for monolithic integration of near infrared laser sources for silicon photonics.

References and links

1. D. Liang and J. E. Bowers, "Recent progress in lasers on silicon," Nat. Photonics **4**(8), 511–517 (2010).
2. J. Liu, X. Sun, R. Camacho-Aguilera, L. C. Kimerling, and J. Michel, "Ge-on-Si laser operating at room temperature," Opt. Lett. **35**(5), 679–681 (2010).
3. R. E. Camacho-Aguilera, Y. Cai, N. Patel, J. T. Bessette, M. Romagnoli, L. C. Kimerling, and J. Michel, "An electrically pumped germanium laser," Opt. Express **20**(10), 11316–11320 (2012).
4. J. Liu, X. Sun, D. Pan, X. Wang, L. C. Kimerling, T. L. Koch, and J. Michel, "Tensile-strained, n-type Ge as a gain medium for monolithic laser integration on Si," Opt. Express **15**(18), 11272–11277 (2007).
5. M. El Kurdi, G. Fishman, S. Sauvage, and P. Boucaud, "Band structure and optical gain of tensile-strained germanium based on a 30 band k·p formalism," J. Appl. Phys. **107**(1), 013710 (2010).
6. M. Virgilio, C. L. Manganelli, G. Grosso, G. Pizzi, and G. Capellini, "Radiative recombination and optical gain spectra in biaxially strained n-type germanium," Phys. Rev. B **87**(23), 235313 (2013).
7. B. Dutt, D. Sukhdeo, D. Nam, B. Vulovic, Z. Yuan, and K. Saraswat, "Roadmap to an efficient germanium-on-silicon Laser: strain vs. n-type doping," IEEE Photonics J. **4**(5), 2002–2009 (2012).
8. L. Carroll, P. Friedli, S. Neuenschwander, H. Sigg, S. Cecchi, F. Isa, D. Chrastina, G. Isella, Y. Fedoryshyn, and J. Faist, "Direct-gap gain and optical absorption in germanium correlated to the density of photoexcited carriers, doping, and strain," Phys. Rev. Lett. **109**(5), 057402 (2012).
9. H. Gamble, B. M. Armstrong, P. T. Baine, Y. H. Low, P. V. Rainey, S. J. N. Mitchell, and D. W. McNeill, *Germanium Processing* (Springer, 2011), pp. 3–29.
10. G. Scappucci, G. Capellini, W. M. Klesse, and M. Y. Simmons, "New avenues to an old material: controlled nanoscale doping of germanium," Nanoscale **5**(7), 2600–2615 (2013).
11. G. Capellini, M. De Seta, P. Zaumseil, G. Kozlowski, and T. Schroeder, "High temperature x ray diffraction measurements on Ge/Si(001) heterostructures: a study on the residual tensile strain," J. Appl. Phys. **111**(7), 073518 (2012).
12. P. Boucaud, M. El Kurdi, A. Ghrib, M. Prost, M. de Kersauson, S. Sauvage, F. Aniel, X. Checoury, G. Beaudoin, L. Largeau, I. Sagnes, G. Ndong, M. Chaigneau, and R. Ossikovski, "Recent advances in germanium emission," Photonics Res. **1**(3), 102–109 (2013).

13. Y. Huo, H. Lin, R. Chen, M. Makarova, Y. Rong, M. Li, T. I. Kamins, J. Vuckovic, and J. S. Harris, "Strong enhancement of direct transition photoluminescence with highly tensile-strained Ge grown by molecular beam epitaxy," Appl. Phys. Lett. **98**(1), 011111 (2011).
14. A. Ghrib, M. de Kersauson, M. El Kurdi, R. Jakomin, G. Beaudoin, S. Sauvage, G. Fishman, G. Ndong, M. Chaigneau, R. Ossikovski, I. Sagnes, and P. Boucaud, "Control of tensile strain in germanium waveguides through silicon nitride layers," Appl. Phys. Lett. **100**(20), 201104 (2012).
15. A. Ghrib, M. El Kurdi, M. de Kersauson, M. Prost, S. Sauvage, X. Checoury, G. Beaudoin, I. Sagnes, and P. Boucaud, "Tensile-strained germanium microdisks," Appl. Phys. Lett. **102**(22), 221112 (2013).
16. V. R. D'Costa, Y.-Y. Fang, J. Tolle, J. Kouvetakis, and J. Menéndez, "Tunable optical gap at a fixed lattice constant in group-IV semiconductor alloys," Phys. Rev. Lett. **102**(10), 107403 (2009).
17. E. Kasper, M. Kittler, M. Oehme, and T. Arguirov, "Germanium tin: silicon photonics toward the mid-infrared," Photonics Res. **1**(2), 69–76 (2013).
18. J. R. Jain, A. Hryciw, T. M. Baer, D. A. B. Miller, M. L. Brongersma, and R. T. Howe, "A micromachining-based technology for enhancing germanium light emission via tensile strain," Nat. Photonics **6**(6), 398–405 (2012).
19. M. J. Süess, R. Geiger, R. A. Minamisawa, G. Schiefler, J. Frigerio, D. Chrastina, G. Isella, R. Spolenak, J. Faist, and H. Sigg, "Analysis of enhanced light emission from highly strained germanium microbridges," Nat. Photonics **7**(6), 466–472 (2013).
20. C. Boztug, J. R. Sánchez-Pérez, F. F. Sudradjat, R. B. Jacobson, D. M. Paskiewicz, M. G. Lagally, and R. Paiella, "Tensilely strained germanium nanomembranes as infrared optical gain media," Small **9**(4), 622–630 (2013).
21. J. R. Sánchez-Pérez, C. Boztug, F. Chen, F. F. Sudradjat, D. M. Paskiewicz, R. B. Jacobson, M. G. Lagally, and R. Paiella, "Direct-bandgap light-emitting germanium in tensilely strained nanomembranes," Proc. Natl. Acad. Sci. U. S. A. **108**(47), 18893–18898 (2011).
22. Y. Yamamoto, G. Kozlowski, P. Zaumseil, and B. Tillack, "Low threading dislocation Ge on Si by combining deposition and etching," Thin Solid Films **520**(8), 3216–3221 (2012).
23. G. Capellini, G. Kozlowski, Y. Yamamoto, M. Lisker, C. Wenger, G. Niu, P. Zaumseil, B. Tillack, A. Ghrib, M. de Kersauson, M. El Kurdi, P. Boucaud, and T. Schroeder, "Strain analysis in SiN/Ge microstructures obtained via Si-complementary metal oxide semiconductor compatible approach," J. Appl. Phys. **113**(1), 013513 (2013).
24. R. Xie, T. H. Phung, M. Yu, and C. Zhu, "Effective surface passivation by novel SiH_4-NH_3 treatment and BTI characteristics on interface-engineered high-mobility HfO_2-gated Ge pMOSFETs," IEEE Trans. Electron. Dev. **57**(6), 1399–1407 (2010).
25. O. Moutanabbir, M. Reiche, A. Hähnel, M. Oehme, and E. Kasper, "Multiwavelength micro-Raman analysis of strain in nanopatterned ultrathin strained silicon-on-insulator," Appl. Phys. Lett. **97**(5), 053105 (2010).

1. Introduction

The realization of a Si-integrated light source represents today the "*Holy Grail*" of silicon photonics. Among different proposed approaches, a laser based on Ge/Si heterostructures is now considered very promising [1]. Indeed, Ge exhibits superior optoelectronic properties with respect to Si and it is now a complementary metal oxide semiconductor (CMOS) foundry-compatible material produced by means of fully qualified fabrication processes.

The recent demonstration of optically [2] and electrically [3] pumped Ge-based laser fabricated on a Si substrate has been welcomed in the scientific community as a leap toward the achievement of a monolithically integrated silicon-based photonic platform. In order to engineer the optical properties of the Ge active material, the authors exploited a combination of moderate biaxial tensile strain ($\varepsilon \sim 2 \times 10^{-3}$) and heavy *n*-type doping ($n_{dop} > 4 \times 10^{19} cm^{-3}$). Germanium is a quasi-direct band gap semiconductor, featuring a Γ_c-L_c valley energy separation of only ~135 meV [4–6]. In tensile strained Ge layers, this energy difference is reduced owing to the different deformation potentials of the conduction band minima, with an indirect-to-direct band gap crossover predicted to occur at $\varepsilon \sim 2 \times 10^{-2}$ [4–6]. A further reduction of the energy barrier, also exploited in [2, 3], is brought about by the filling of the L_c valley by doping electrons. As a result, the transfer of electrons from the low-lying L_c valley to the Γ_c valley is facilitated, with a consequent increase of the direct bandgap recombination, leading in turn to optical gain [6]. Unfortunately, the device demonstrated by Camacho-Aguilera et al. suffered of extremely high lasing threshold current density [3], which limited its operating lifetime to few minutes. In order to address this major issue, two different routes can be considered: ultra-high doping density and/or increased tensile strain [7].

Increasing the doping density can be convenient since it induces a super-linear increase of the carrier density present in the conduction band Γ_c valley and, consequently leads to an increased radiative recombination rate. Though, this advantage is counterbalanced by the enhanced free carrier absorption and non-radiative recombination rate, which could actually hinder the lasing at all [8]. Moreover, the achievement of a heavy n-type doping has proven to be difficult in Ge, owing to low solubility, fast diffusion, and limited activation of the dopants [9, 10].

Consequently, band engineering through application of higher tensile strain appears to be more promising since it has in principle no drawbacks in terms of extra optical losses. However, the tensile strain values directly achievable by exploiting the difference between the coefficients of thermal expansion in Ge and Si during the Ge/Si growth, as in the approach pursued in [2,3], is limited to a mere $\varepsilon_{therm}{<}2.5 \times 10^{-3}$ [11]. In order to go beyond this value, different strategies based on heteroepitaxy or micromachining have been recently proposed and relatively high values uniaxial and biaxial strain obtained (up to $\varepsilon{\sim}0.015$, see [12] for a review). Nevertheless, the proposed methods rely either on non CMOS-qualified materials (such as Ge on III-V substrates [13–15] or Ge on GeSn alloys [16,17]), or on fabrication schemes leading to microstructures having shape and/or sizes which prevents their embedding in Fabry-Perot laser cavities [18–21]. Consequently these methods appear, although very interesting from a fundamental point of view, difficult to integrate into the CMOS silicon environment, at least on the short-medium term.

In this work we demonstrate a CMOS based fabrication approach to obtain Ge microstripes on Si wafer with equivalent biaxial tensile strain values up to $\varepsilon \sim 9 \times 10^{-3}$. The tensile strain field is induced by the elastic relaxation, occurring after the lithographic definition of the microstructure, of a compressively strained SiN layer deposited on top of a Ge/Si heterostructure. Our structures have a spatially homogeneous strain distribution which can be in principle extended over any arbitrary length. The achieved tensile strain leads to an enhancement of the photoluminescence intensity of more than an order of magnitude, with respect to the thermally strained Ge. The shape of the fabricated microstructures has been chosen in view of their possible use as active lasing material in linear Fabry-Perot cavities. Our numerical results indicate that in 1 mm-long microstripes robust modal gain can be achieved at relatively low excess carrier density.

2. Experimental and theoretical methods

The microstructures here studied were fabricated out of a SiN/Ge/SOI(001) stack in a 130-nm Bi-CMOS fabrication line using standard qualified processes. After a proper cleaning of 200-mm SOI wafers (top silicon thickness = 80 nm, buried oxide (BOX) thickness = 2 μm), the epitaxial growth of a 450 nm-thick Ge layer was carried out in a single wafer reduced pressure-chemical vapor deposition (RP-CVD) system, using H_2-diluted GeH_4 in a two-temperature deposition process. In order to improve Ge crystal quality, cyclic annealing at 800 °C was performed by interrupting the Ge deposition [22]. A threading dislocation density of $\sim 1 \times 10^6$ cm^{-2} was evaluated using the etch pit count technique. Subsequently, a 450-nm thick SiN stressor was deposited on top of the Ge layer by plasma-enhanced CVD using a SiH_4-NH_3-N_2 mixture. The SiN layer deposition parameters were selected to maximize the residual *compressive* stress σ_{SiN} in the stressor layer. A value of $\sigma_{iN} = -2.5$ GPa was obtained. To avoid chucking issues during the fabrication process, induced by the stress driven wafer bowing, a SiN compensating stressor was deposited on the wafer backside.

The strain relaxation of the microstructures was modeled using COMSOL Multiphysics 4.2, a 3D finite element (FEM) tool. The Ge and Si layers in the stack were defined anisotropic, with a residual strain of $\varepsilon_{therm} = 2.5 \times 10^{-3}$ as initial condition for Ge, in order to account for the presence of the thermal strain. The SiN stressor layer and the buried oxide (BOX) were defined as isotropic. Fixed boundary was set for the BOX, allowing the rest of

the structure to deform freely. The experimental value for σ_{SiN} (−2.5 GPa) was used as initial condition for the SiN stressor layer.

Micro-Raman measurements were performed in order to evaluate the elastic strain in the micro-structures. We have used an InVia Renishaw spectrometer working in backscattering geometry with a laser focal spot of ~0.8 μm in diameter and a 100 × objective lens with a numerical aperture of 0.85. Three laser wavelengths were used: 633 nm, 514 nm, and 488 nm. The laser power was low enough to prevent heating, as proved by monitoring the peak position of the Raman Ge-Ge mode over long acquisition time. Each microstructure was characterized by measurements along the mid line of its the longitudinal axis. To get a reference signal, measurements were extended also in the unpatterned stack region. The Raman shift of the Ge-Ge mode $\omega_{Ge\text{-}Ge}$ in the micro-structures was measured with respect to the Ge-Ge phonon mode energy $\omega^0_{Ge\text{-}Ge}$, measured on a Ge(001) reference bulk crystal ($\omega^0_{Ge\text{-}Ge}$ = 300.17 cm^{-1}). The equivalent in-plane biaxial strain, defined as $\varepsilon^{bi} = (\frac{\varepsilon xx + \varepsilon yy}{2})$, was calculated using the relationship $\varepsilon^{bi} = (\frac{\omega_{Ge-Ge} - \omega^0_{Ge-Ge}}{-390})$ [23].

The room temperature emission of the microstructures was measured by means of a micro-photoluminescence (μ-PL) set-up, using a cw-HeNe laser at 633 nm pump, focused on the sample with a × 50 objective having a numerical aperture of 0.8. The emission was dispersed by an iHR 550 Horiba Jobin-Yvon spectrometer and measured with a liquid nitrogen cooled extended InGaAs detector array. The incident power density impinging on the microstructure was estimated to be ~2 × 10^4 W cm^{-2}. Since all the investigated structures belong to a single wafer, all the measurements have been performed exactly in the same alignment conditions, leading to a meaningful comparison of measured spectral intensity.

The optical properties of the strained Ge material were calculated using the model developed in [6] by Virgilio et al. to evaluate radiative recombination rates and material absorption/gain coefficients in biaxially strained intrinsic and n-type Ge layers. To this aim, both direct and indirect radiative transitions have been considered, together with the different contributions to the optical spectra originating from heavy holes (*HH*), light holes (*LH*), and split-off valence bands. Similarly to what previously reported in the literature, the strain induced split of the *HH* and *LH* levels at the Γ_v point, and more generally the effects of the strain field on the different band edges, have been taken into account [2,19]. Furthermore, the effect of the lattice distortion on the band curvatures, which in turns influence the excess carrier energy distribution, and on the dipole matrix element, which is a key parameter for a sound estimation of the gain spectra, was fully considered in our numerical simulations. It is worth notice that an erroneous underestimation of these latter effects may lead to overestimate the radiative recombination rates [6].

Finally, the modal gain has been addressed by calculating the gain dependence as a function of strain and wavelength and by numerical evaluation of the overlap of this gain profile with the optical mode and of Fabry-Perot cavity losses.

3. Results

In Fig. 1(a) we present a Scanning Electron Microscopy (SEM) image of the wafer surface showing microstructures of the two types here investigated. The "I" structures were obtained removing, down to the BOX surface, the material from the region surrounding the defined microstripe, having width w (y axis) and length l (x axis*)*. In this configuration the stripe is only connected to the surrounding at its bottom. Type "H" structures were instead obtained leaving the microstripe attached to the surrounding unpatterned region at the two ends of its longitudinal axis x. Data related to H- and I- type structures will be labeled throughout this article in blue and red, respectively.

In Fig. 1(b) a SEM image of a section along the (*y,z*) plane of a typical microstripe carved by focused ion beam (FIB) has been displayed. The Ge and SiN thickness were selected accordingly to electromagnetic simulations in order to provide a good TE and TM confined mode with strong overlap with the Ge layer over the entire range of width investigated. In order to study the impact of geometry on strain and optical properties, the width *w* was varied in the [1 ÷ 10] μm range and the length *l* in the [10 ÷ 150] μm range, for both I and H structures. Structures aligned both along [100] and [110] crystallographic orientations were fabricated in order to verify the impact of uniaxial strain applied along different directions [14]. As an example, in Fig. 1(c) we present the model geometry used to simulate an "H" structure in FEM calculations together with the chosen orientation of the reference system.
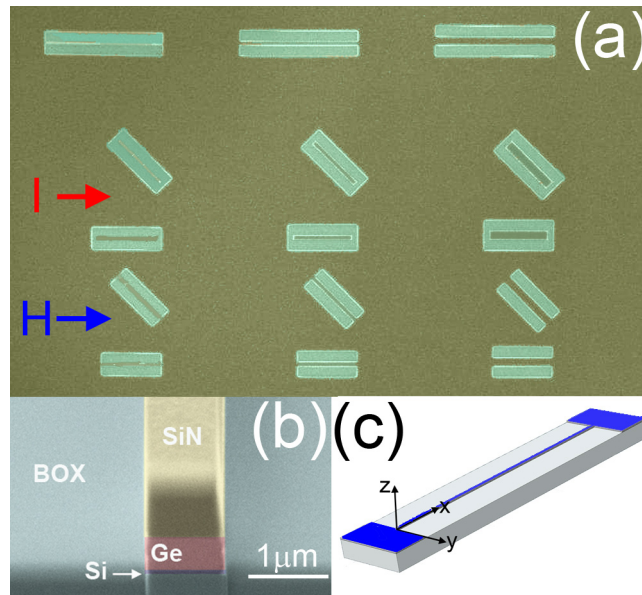

Fig. 1. (a) SEM image of representative CMOS-fabricated microstripes; [110]-oriented (parallel to the image side) and [100] (45° rotated) "I" and "H" structures are visible. (b) SEM image of a FIB cross section performed on 1 μm wide microstripe revealing its layered structure; (c) COMSOL scheme used to model the strain distribution in H structures. The origin of the *z*-axis is set at the Ge/Si interface.

The unpatterned Ge layer featured, after the completion of the entire SiN/Ge/SOI stack, an average biaxial tensile strain ε_{therm} = 2.5 × 10^{-3}, as measured by XRD and μ-Raman spectroscopy, originated during the deposition process by the different thermal expansion coefficients of Ge and Si [11]. When patterned, the SiN stressor "pulls" sideways the underlying Ge film generating a strain distribution within the layered microstripe. In Fig. 2(a) we plot the distribution of the equivalent biaxial strain ε^{bi}, as obtained by a projection on the (*x* = 10 μm, *y*, *z*) plane of data from a full FEM calculations performed on a *w* = 2 μm wide, *l* = 20 μm long H-type structure. We can see that the elastic relaxation of the compressive stress induces a tensile strain field in the SiN stressor layer which, in turn, causes a strain distribution in the underlying Ge/SOI region. We notice that the tensile strain is maximized at the SiN/Ge interface and increases from the sidewalls toward the longitudinal central axis. The strain distribution shown, although quantitatively dependent on the type and size of the micro-stripes, qualitatively captures a general trend as observed in all the investigated structures. It is remarkable that this distribution is highly beneficial to maximize the net optical gain in light emitting photonic devices. As a matter of fact, where the tensile strain values are higher, the Ge band gap is narrower [4–6]. As a consequence electron and holes are "funneled" by the strain-originated built-in effective electrical field towards the top Ge

surface region, close to the SiN/Ge interface exactly where the spontaneous radiative recombination rate is higher [6]. At the same time excess carriers are driven away from the bottom Ge/Si interface where the heteroepitaxial misfit dislocations are located. As a consequence the non-radiative recombination of electron-hole pairs caused by these extended defects can be decreased. Moreover, the SiN stressor layer acts also as effective surface passivation layer [24], resulting in a reduced surface recombination velocity of carriers, and thus reduced non-radiative losses.
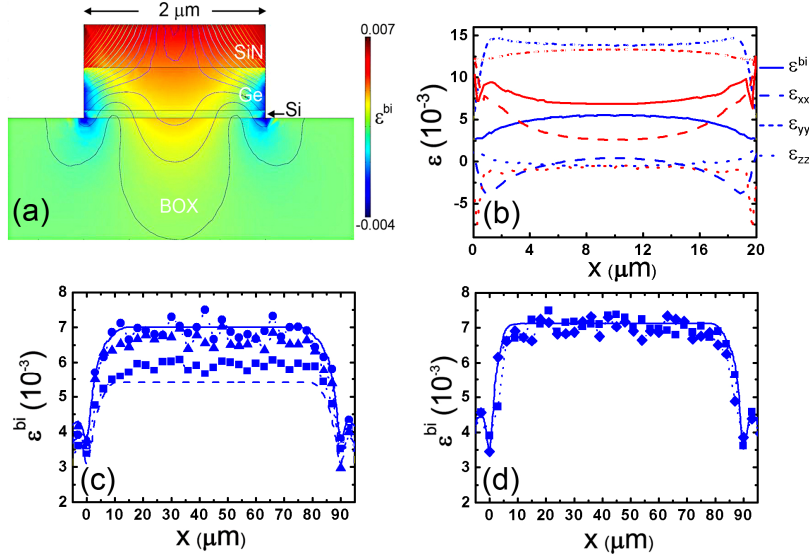

Fig. 2. (a) Equivalent biaxial strain values as calculated in a (y,z) plane at the center ($x_c = 10$ μm) of a 20 μm long and 2 μm wide H-type Ge microstripe. Isolines describe the displacement field due to the stress relaxation. (b) Diagonal components of the strain tensor calculated at the SiN/Ge interface along the x-axis of a H-type (blue) and a I-type (red) microstructure having $w = 2$ μm and $l = 20$ μm. The resulting equivalent biaxial strain is reported as continuous line. (c) Strain profile along the x axis of a $w = 2$ μm, $l = 90$ μm H-type microstructure as measured by μRaman using a laser wavelength of $\lambda = 488$ nm (circles), $\lambda = 514$ nm (triangle), or $\lambda = 633$ nm (square). We also display the calculated strain profile at the SiN/Ge interface (continuous line) or 225 nm below this (dashed line). (d) Strain profile obtained by μ-Raman ($\lambda = 514$ nm) on a $l = 90$, $w = 2$ H-type oriented along [110](square) and [100] (diamond) and from simulation (values at the SiN/Ge interface, solid line)

More insight in the strain distribution can be gained from Fig. 2(b) where we plot the diagonal components of the strain tensor, calculated at the SiN/Ge interface and along the x-axis of two $w = 2$ μm and $l = 20$ μm H- and I-type structures, together with the resulting equivalent biaxial strain value ε^{bi}. For both structure types, the strain is mostly uniaxial with the ε_{yy} values much larger than those corresponding to the other components. This can be attributed to the elongated microstructure geometry. In fact, while every transverse portion of the stripe is free to expand laterally in the y-direction, the strain relaxation along the x-axis is hindered by the presence of the neighboring segments of the stripe. This effect is particularly evident comparing the ε_{xx} profiles at the boundary of I-and H-type structures along the longitudinal axis. While in the former case the two end facets are free to expand outwards in x (ε_{xx} increases close to $x = 0$ and $x = 20$ μm in Fig. 2 (b) the opposite holds in the latter case, owing to the compressive action generated by the surrounding unpatterned material which "pushes" along x against the microstripe. The two different relaxation behaviors are observable also in the ε^{bi} strain profile, which shows at the ends an increasing value of the tensile strain only for I-type microstripes. Remarkably, for relatively long structures (l>40 μm) the equivalent biaxial strain distribution is homogenous along the x-axis. This can be

seen in Fig. 2 (c) where we plot ε^{bi} calculated at the SiN/Ge interface ($y = 0$, continuous line) along the x-axis for a $w = 2$ μm, $l = 90$ μm H-type microstructure. We notice that distributions for ε^{bi} are found to be homogeneous along x at each height z, and with decreasing values from the top to the bottom of the Ge layer, as evident in Fig. 2(a). As an example the ε^{bi} field, calculated at the mid height of the Ge region ($y = 0$, $z = 225$ nm; dashed line) is reported in Fig. 2(c). For comparison, we show in Fig. 2(c) also the experimental strain values, measured by μ-Raman with an excitation laser wavelength of 488 nm (circle), 514 nm (triangle), or 633 nm (square). In highly absorbing material such as Ge, the Raman signal comes from a narrow volume defined by the light penetration depth Λ, the spot size, and the field depth. As a consequence, Raman measurements performed at different wavelengths provide information on strain at different distance from the surface [25]. The strain data, obtained with 488 nm and 514 nm wavelengths, which feature nearly identical light penetration depths ($\Lambda \sim 17$ nm), are in good agreement with the strain values at the SiN/Ge interface predicted by the FEM calculation; on the other hand measurements acquired using as excitation the 633 nm wavelength, featuring an absorption length $\Lambda_{633} = 64$ nm, are best suited to probe the strain distribution deeper into the Ge film and, at least qualitatively, confirm the numerical z-dependence of the biaxial strain distribution shown in Fig. 2(a). It is worth noting that the observed and calculated strain distributions do not change if the structure main axis is aligned along the [110]- (square) or [100]-equivalent (diamonds) crystallographic directions, as clearly visible in Fig. 2(d) where we display the Raman-derived strain values obtained for two $l = 90$, $w = 2$ H-type microstructures.

We now discuss the light emission properties of the investigated microstructures. The room temperature photoluminescence spectra, acquired at the center ($x_c = l/2$; $y_c = 0$) of H-type and I-type microstructures are shown in Figs. 3(a) and 3(b), respectively. Spectra for microstripes having width $w = 2$ μm and different lengths are displayed. In the present experimental configuration, i.e. backscattering geometry, the emission is dominated by a broad peak, corresponding to the electron-hole radiative transitions near the Brillouin zone center $\Gamma_c \rightarrow \Gamma_v(HH)$, occurring across the Ge direct gap and involving holes hosted in the HH band.
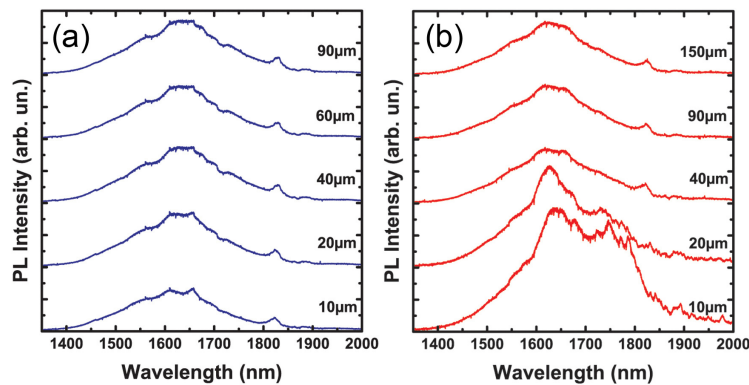

Fig. 3. PL measurements on microstripes having w = 2 μm and lengths as indicated in the plots: (a) H structures, (b) I structures; the curves have been offset for clarity. The signal amplitudes are on the same scale.

The emission is partly modulated by Fabry-Perot modes. While the peak resonances observable at a wavelength of ~1660 nm and ~1830 nm result from the lateral width, the small resonance at ~1890 nm corresponds to a Fabry-Perot mode associated with the vertical stacking of the layers. For the 10 μm- and 20 μm-long I-type microstructures, an additional shoulder is observed at ~1790 nm. We attribute it to the indirect band recombination $L_c \rightarrow \Gamma_v(HH)$ and, possibly, to direct transitions involving the LH valence band. We notice

that, although the hole states close to the LH band edge are energetically favorite, the PL signal related to $\Gamma_c \rightarrow \Gamma_v(LH)$ transitions does not dominate the PL spectrum since its squared dipole matrix element for TE photon emission is a factor of ~5 smaller than the one involving HH holes. As a consequence, the $\Gamma_c \rightarrow \Gamma_v(LH)$ recombination becomes dominant only at higher strain levels and much lower excitation power [21]. For long structures ($l > 40$ µm), the peak maximum wavelength is found at λ_{peak} ~1620-1625 nm, and does not significantly depend on the length, as apparent from Fig. 4(a). This large red-shift with respect to the peak emission wavelength of bulk Ge ($\lambda_{Ge} = 1530$ nm) results from the direct gap shrinking caused by the tensile strain, which in both I and H microstripes saturates for $l > 40$ µm at about ε^{bi} ~7×10^{-3}.
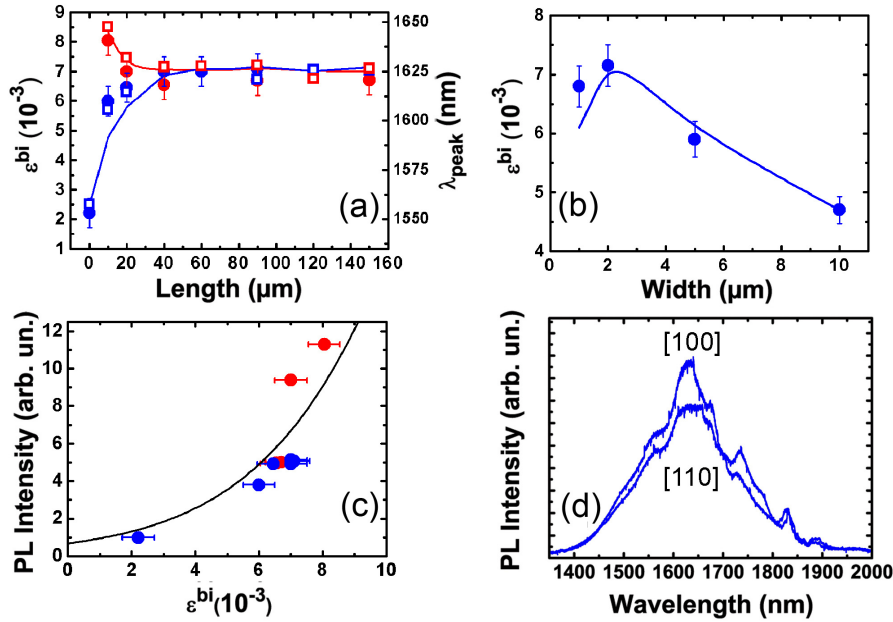

Fig. 4. (a) Equivalent biaxial strain as predicted by COMSOL simulation at the SiN/Ge interface (solid lines), obtained by PL measurement (filled symbols), and µ-Raman (open) for H (blue) and I structures (red) having $w = 2$ µm and different lengths. On the right axis the corresponding peak energy are also reported. The point at $l = 0$ represents the unpatterned region; (b) equivalent biaxial strain as predicted by COMSOL simulations at the SiN/Ge interface (solid line) and obtained by PL measurement (circle) as a function of the width in H-structures with $l = 90$ µm. (c) Dependence of the integrated PL intensity as a function of biaxial strain. The solid line corresponds to the modeling results. (d) PL spectra obtained on two H-type structures having $w = 2$ µm $l = 90$ µm and the different x-axis orientations.

The strain stability with respect to the microstripe length indicates that the process is robust and the approach scalable. It follows that a tensile strain of 7×10^{-3} can in principle be achieved also in millimeter long structures which are required for both lasing and high emitted optical power. For short microstripe lengths ($l < 40$ µm), H-type and I-type microstructures show opposite behaviors. In this case, for decreasing length, the photoluminescence peak wavelength red shifts for H-type structures and has a decreasing intensity. Conversely, in I-type structures it is blue-shifted and has an increased intensity. From the above discussion it is clear that the PL peak energy position can be used to measure the strain in the Ge layer [5,6]. To this aim, values for the equivalent biaxial strain in microstripes with different geometries have been estimated by matching the strain-driven variation of the Ge direct gap with the energy red-shift of the PL peak [6,14]. Notice that, due to the aforementioned funneling effect, the excess electron-hole pairs are mainly located at the SiN/Ge interface. As a consequence, also the PL measurements are mainly affected by the strain field existing in this region. For this reason, the dependence of the biaxial strain

obtained in I and H structures from the PL spectra as a function of the microstripe length (closed symbols) is compared in Fig. 4(a) with the "surface-sensitive" Raman measurements acquired using the λ = 514 nm excitation light (open symbols). In the same figure we also show the FEM strain values calculated at the SiN/Ge interface for x_c = l/2 and y_c = 0 (solid line). A very good agreement is obtained between both the experimental techniques and the numerical data.

In Fig. 4(b) we report the equivalent biaxial strain values as obtained by PL measurements at the center of H structures having l = 90 µm and different width w. We also display (solid line) the theoretical strain values calculated by FEM at the SiN/Ge interface and at the center of the structure (x_c = 45 µm, y_c = 0). By decreasing the microstripe width down to w = 2 µm the strain increases for both H and I structure (not shown) in an identical manner. Below this width the strain begins to decrease. This behavior, counter-intuitive at a first glance, can be understood by closely inspecting Fig. 2(a). Upon decreasing the width, the two compressive regions existing at the lateral edges of the Ge/Si interface, originated by the outward bending of the stripe sidewalls, extend more towards the center of the structure and better contribute to reduce the tensile strain value at the SiN/Ge interface.

The integrated PL intensities, obtained from the spectra of Figs. 3(a) and 3(b), are reported in Fig. 4(c) as a function of the equivalent biaxial strain, evaluated from the PL peak energy. The PL intensity shows a super-linear increase with ε^{bi}. At ε^{bi} = 7 × 10^{-3} we observe an enhancement of a factor of ~12 with respect to ε_{therm} = 2.5 × 10^{-3}, i.e. the strain featured by the Ge active material in the optical and electrically pumped laser by MIT group [2,3].

This super-linear behavior is very well described by our theoretical modeling, whose results are displayed as a solid line. The theoretical data have been obtained calculating the emitted PL flux from a semi-infinite intrinsic Ge material, characterized by a spatially independent biaxial strain field, optically excited by a steady state monochromatic radiation source with the experimental wavelength and power density, impinging normally to the sample surface. Since in our experiments the optical excitation is spatially localized close to the top Ge surface, where the strain field has its highest positive values, self-absorption effects, which in general may be responsible for differences between the PL and the bare radiative recombination rate spectra, can be neglected in the present contest. Therefore, the PL flux is simply proportional to the angular and energy resolved recombination rate spectrum, which has been calculated for photons emitted along the observation direction. We notice here that the "funneling" effect also justify the modeling of our structures with a semi-infinite material and a spatial-independent biaxial strain field which is set equal to the one measured at the SiN/Ge interface. The peak values of the excess electron-hole concentrations have been calculated for our experimental excitation conditions taking in to account the contributions from both radiative and non-radiative recombination channels (see [6]). We find that they are quite insensitive to the strain variation and remains of the order of 1x10^{19} cm^{-3} when ε^{bi} is varied in the [0 ÷ 9 × 10^{-3}] interval. Most of the excess electrons occupy the L_c degenerate valleys owing to their lower energy and larger density of state compared to the non-degenerate, light mass Γ_c valley [6]. However, increasing the strain from 0 to ~9 × 10^{-3}, the room temperature excess carrier density in the conduction Γ_c valley dramatically increases from 8 × 10^{14} cm^{-3} to 1.2 × 10^{16} cm^{-3} due to the strain-driven lowering of the Γ_c -L_c energy barrier. The resulting electron transfer from the L_c- toward the Γ_c valley increases the number of active radiative direct transitions and it is responsible for the observed enhancement of the PL signal. Moreover, our numerical results confirm that the main peak of the PL intensity is to be associated with direct recombinations involving holes hosted in the HH band. Indeed, although in tensile strained Ge this band has higher energy with respect to LH, the oscillator strength for photons emitted along the (001) direction is higher when HH holes are involved.

In Fig. 4(d) we display the PL spectra of two H-type structures having w = 2 µm and l = 90 µm, oriented either along the [110] or [100] directions. The latter structure exhibits a peak intensity ~1.4 × compared to its [110]-oriented counterpart. As can be observed, the two

structures have the same peak energy, meaning an identical value of the equivalent biaxial strain, as confirmed by the direct strain analysis performed by μ-Raman (see Fig. 2(d)). Thus the intensity increase observed in the [100] oriented microstripes cannot be attributed to larger biaxial equivalent strain values. This feature is instead caused by the different effect of the uniaxial strain component on the L_C degenerate valleys when it is applied along the [100] or [110] directions. As clearly seen in Fig. 2(b), the stripe geometry induces a uniaxial strain oriented perpendicular to the structure x-axis. If this axis is aligned to the [110] direction, the uniaxial strain induces a lift of the L_C degeneracy accompanied by an average increase of the Γ_c -L_c energy barrier [14]. On the contrary, a uniaxial strain along an equivalent [100] direction leaves the valley degeneracy unaltered. As a consequence, for a given value of strain, the excess electron occupation of the Γ_c valley is higher in the [100] case. This fact is reflected in an increased PL intensity. For the strain value of the samples in Fig. 4(d), we could estimate a PL intensity ~1.5x higher than in the [110] case [14], in very good agreement with our observations.

4. Discussion

Once the reliability of our model has been established by comparison with the experiments, we shall use it in a predictive way to maximize the optical gain in the experimentally accessible parameter space of strain, doping, and excess carrier concentration. To this aim we first notice that, as one may expect from the above results, the material gain is an increasing function of the biaxial strain. Moreover, from the analysis of the numerical data reported in [6], one can conclude that the optical gain increases upon increasing the n-type doping concentration. This result is not trivial since large doping density, if on one hand eases the transfer of electron towards the Γ_c valley, on the other has the drawback of increasing the optical losses due to free carrier absorption. To correctly account for the free carrier absorption at high doping and excitation density both in the valence and conduction band, we relied on the wavelength- and concentration dependent loss function proposed by Carroll and associates [8] for electrons and the one proposed in [4] for holes. In our simulation we used the maximum strain achievable in arbitrary long structures ($\varepsilon^{bi} = 7 \times 10^{-3}$) and $n_{dop} = 4 \times 10^{19}$ cm^{-3}, being this latter quantity a large but still realistic value for the doping concentration achievable in our systems, lower than the doping density used by Camacho-Aguilera and associates in their light emitting structures [3]. Our numerical results are reported in Fig. 5, where we show TE and TM optical gain spectra calculated at room temperature for different values of the excess carrier concentration δn, ranging in the $[1 \div 10] \times 10^{18}$ cm^{-3} interval, i.e. a range close to the one estimated for our PL experimental conditions. A robust material gain can be achieved both for TE and TM, with peak value increasing with the excess carrier density. For $\delta n = 1 \times 10^{19}$ cm^{-3} the TE (TM) gain peak value is ~300 (700) cm^{-1} and occurs at the emission wavelength of 1650 (1765) nm, corresponding to the Γ_c-Γ_v(HH) (Γ_c-Γ_v(LH)) energy gap. We notice here that the Hartree-Fock screening can induce a band-gap narrowing of few tens of meV for n-type doping density in the 10^{19} cm^{-3} range which has not considered in our model. However the energy difference between L_c and Γ_c valleys is nearly independent of doping [4]. Therefore, neglecting the bandgap shrinkage due to doping does not affect the spectral gain evaluation except that the gain peak may be slightly blue-shifted.

The two light polarizations TE and TM are not equivalent since the strain field breaks the cubic symmetry of the lattice structure. As a consequence, the direction of the polarization vector of the guided electromagnetic mode can be exploited as a further degree of freedom to maximize the emission intensity by engineering the laser cavity geometry. If a biaxial tensile strain field is applied to a Ge layer, the material gain peak in the TM mode is larger than that achievable with in-plane polarization vector [6]. This is due to the fact that the oscillator strength in the TM mode is completely transferred to the Γ_c -Γ_v(LH) transition, while for TE polarization it is shared also with the Γ_c-Γ_v(HH) transition, occurring at a different energy. It follows that, since both HH and LH levels are populated at room temperature, the spectral

region where the TE absorption coefficient is low is quite large, while in TM polarization it is concentrated around the Γ_c -$\Gamma_v(LH)$ gap (see Fig. 5). As a consequence, larger peak gain values can be achieved in this latter case.

The main issue for these tensile microstructures is to know whether they could achieve lasing or not. To this aim, we have calculated the modal gain for realistic values of n-doping and photo-induced carrier densities. We take into account the inhomogeneous strain profile along the z vertical direction as shown in Fig. 2. For simplicity, we suppose that the photo-induced carrier density is uniformly distributed in the germanium volume. This is obviously a simplification as the variation of strain induces a variation of band gap energy and modifies the carrier distribution. The material gain was calculated for different values of strain, thus providing, at a fixed wavelength, the spatial behavior of the gain on the vertical direction. The overlap of the material gain with the mode profile is then computed to obtain the modal gain. We emphasize that the presence of the BOX is very advantageous for the modal confinement. For a n-type doping of $n_{dop} = 2 \times 10^{19}$ cm^{-3} and a photo-induced generation of $\delta n = 1 \times 10^{19}$ cm^{-3}, the modal gain remains negative over the whole spectral range (-177 cm^{-1} at 1650 nm). If we increase the doping density up to $n_{dop} = 4 \times 10^{19}$ cm^{-3}, the modal gain becomes positive (50 cm^{-1} at 1720 nm for $\delta n = 5 \times 10^{18}$ cm^{-3} and 130 cm^{-1} at 1650 nm for $\delta n = 1 \times 10^{19}$ cm^{-3}). This switch from negative to positive gain depends on the profile of the photo-induced carrier density. If we consider an $L = 1$ mm long waveguide and the Ge/air interface characterized by a reflectivity R, we can estimate the cavity mirror losses to be $\dfrac{1}{2L \ln R^2}$ ~10 cm^{-1}. The waveguide propagation losses due to scattering have also to be considered.

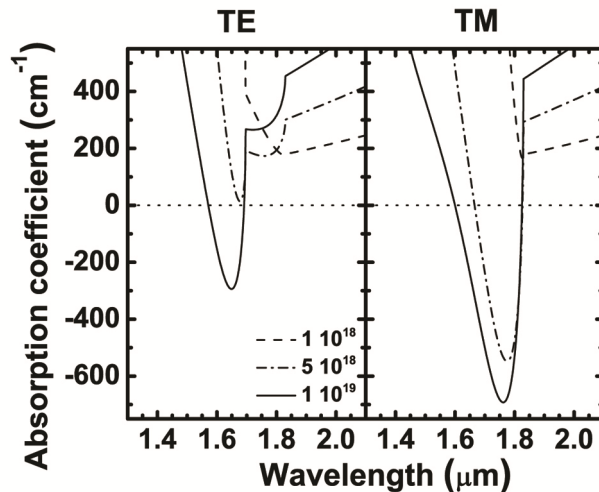Fig. 5. Spectral absorption coefficient calculated for $\varepsilon^{bi} = 7 \times 10^{-3}$ and $n_{dop} = 4 \times 10^{19}$ cm^{-3}, in both TE (left) and TM (right) polarizations and for the different excess carrier densities δn reported in the left panel (cm^{-3}).

Propagation losses of 10 dB·mm^{-1} correspond to losses of ~20 cm^{-1}. This is a conservative estimate as propagation losses could be minimized by optimizing the fabrication process. The modal gain for the doping and injection conditions here considered is thus sufficient to achieve lasing at ~1700 nm in a Fabry Perot cavity, since the modal gain is larger than the sum of reflectivity and propagation losses. Lasing is then obtained for a reasonable carrier injection of $\delta n = 5 \times 10^{18}$ cm^{-3}, a value lower than that needed by Camacho-Aguilera et al. to operate their electrically pumped laser [3].

5. Concluding remarks

In summary, we have demonstrated that CMOS-fabricated Ge-based microstructure can be practically used to achieve an infrared laser monolithically integrated on Si. Our method enable the fabrication of mm-long Fabry-Perot structures with homogeneous strain distribution throughout the length of the whole active layer, thus allowing to achieve high optical output powers of the light emitting device, with on-chip real estate being the only limiting factor. The relatively high biaxial tensile strain obtained allows a significant reduction of laser threshold, still using a technologically available n-type doping concentration. Moreover, we underline that the microstripe geometry and their fabrication process is compatible with electrical injection realizable through standard electrical via connections. The excellent agreement between modeling and measurements shown here, on one hand witnesses the high degree of control that is achieved on the active material properties, on the other hand can be reliably used in the forthcoming design of the laser prototype structures.